AN INVESTIGATION INTO BANDWITH EXPANSION AND SIGNAL INTEGRITY OF FREQUENCY-MULTIPLIER-LAST TRANSMITTERS

by

ÖMER RASİM KINACI

Submitted to the Graduate School of Engineering and Natural Sciences

in partial fulfillment of

the requirements for the degree of Master of Science

Sabancı University

March 2025

AN INVESTIGATION INTO BANDWIDTH EXPANSION AND SIGNAL INTEGRITY IN FREQUENCY-MULTIPLIER-LAST TRANSMITTERS

Approved by:

Asst. Prof. KORKUT KAAN TOKGÖZ: …….
(Thesis Supervisor)

Asst. Prof. MOHANED CHRAITI: ……

Prof. MEHMET ÜNLÜ: ……

Date of Approval: March 20, 2025

ABSTRACT

AN INVESTIGATION INTO BANDWIDTH EXPANSION AND SIGNAL INTEGRITY OF FREQUENCY-MULTIPLIER-LAST TRANSMITTERS

ÖMER RASİM KINACI

Electronics Engineering, M.Sc. Thesis, 2025

Thesis Supervisor: Asst. Prof. KORKUT KAAN TOKGÖZ

Keywords: Frequency Multipliers, Digital Communications, sub-THz transmitters

The evolution of wireless communications necessitates transmitters capable of achieving data rates in the range of tens of gigabits per second. Due to high congestion and strict regulations, lower-frequency bands are unlikely to satisfy the growing data-rate demands set by regulatory bodies such as the International Telecommunication Union (ITU). Consequently, sub-THz frequencies (above 100 GHz) are being explored as viable alternatives for high-speed wireless communication.

However, the relatively low maximum operating frequencies of CMOS transistors pose limitations for conventional transmitter architectures, which typically rely on power amplifiers in their final stage. To address this challenge, frequency-multiplier-last transmitters have been proposed, enabling efficient frequency upconversion to sub-THz bands using solely CMOS technology. Despite their advantages, these transmitters introduce significant distortions due to the frequency multiplier stage, negatively impacting digital communication performance.

This thesis presents a mathematical system-level analysis of these impairments. The analysis demonstrates that even-order multipliers are inadequate for supporting digital IQ modulation-based communication between the transmitter and receiver. It further reveals that the signal-to-noise ratio (SNR) degrades proportionally to the square of the multiplier order. The thesis concludes that the frequency tripler is the most suitable option for digital communication in frequency-multiplier-last transmitters.

ÖZET

FREKANS ÇARPANININ SON KADEMEDE BULUNDUĞU VERİCİLERDE BANT GENİŞLEMESİ VE SİNYAL BÜTÜNLÜĞÜNÜN İNCELENMESİ

ÖMER RASİM KINACI

Elektronik Mühendisliği, Yüksek Lisans Tezi, 2025

Tez Danışmanı: Dr. Öğr. Üyesi KORKUT KAAN TOKGÖZ

Anahtar Kelimeler: Frekans Çarpanları, Dijital Haberleşme, sub-THz vericileri

Kablosuz iletişimin evrimi, onlarca Gb/s veri hızlarına ulaşabilen vericileri zorunlu kılmaktadır. Yüksek yoğunluk ve sıkı düzenlemeler nedeniyle, Uluslararası Telekomünikasyon Birliği (ITU) gibi kuruluşların belirlediği artan veri hızı gereksinimlerini düşük frekans bantlarının karşılaması pek olası değildir. Bu nedenle, 100 GHz'in üzerindeki alt-THz frekansları, yüksek hızlı kablosuz iletişim için uygulanabilir bir alternatif olarak araştırılmaktadır.

Bununla birlikte, CMOS transistörlerin görece düşük azami çalışma frekansları, son kademesinde güç yükselteci bulunan geleneksel verici mimarileri için sınırlamalar oluşturur. Bu sorunu aşmak amacıyla, yalnızca CMOS teknolojisi kullanarak alt-THz bantlarına verimli frekans yukarı dönüştürme sağlayan frekans-çarpan-son vericiler önerilmiştir. Ancak bu vericiler, frekans çarpanı kademesinin neden olduğu önemli bozulmalar nedeniyle dijital iletişim performansını olumsuz etkilemektedir.

Bu tez, söz konusu bozulmaları matematiksel bir sistem düzeyi analiziyle incelemektedir. Analiz, çift mertebeli çarpanların verici ve alıcı arasında dijital IQ modülasyonuna dayalı iletişimi desteklemede yetersiz kaldığını göstermektedir. Ayrıca, sinyal-gürültü oranının (SNR) çarpan mertebesinin karesiyle orantılı olarak azaldığını ortaya koymaktadır. Tez, dijital iletişim için frekans üçleyicinin frekans-çarpan-son vericilerde en uygun seçenek olduğu sonucuna varmaktadır.

TABLE OF CONTENTS

LIST OF TABLES

LIST OF FIGURES

LIST OF ABBREVIATIONS

3GPP	3rd Generation Partnership Project
ACPR	Adjacent Channel Power Ratio
AWGN	Additive White Gaussian Noise
BPF	Bandpass Filter
BPSK	Binary Phase Shift Keying
CMOS	Complementary Metal Oxide Semiconductor
DAC	Digital to Analog Converter
DSP	Digital Signal Processing
DPD	Digital Predistortion
EVM	Error Vector Magnitude
f_{max}	Maximum Operating Frequency
Gbps	Gigabits per second
GHz	Gigahertz
GSps	Gigasamples per second
HPF	Highpass filter
IMT	International Mobile Telecommunication
IQ	In-phase Quadrature
ITU	International Telecommunication Union
LO	Local Oscillator
LPF	Lowpass filter
OOK	On-Off Keying
P_{out}	Output Power
PA	Power Amplifier
PRBS	Pseudo-Random-Bit-Sequence
PSK	Phase Shift Keying
QAM	Quadrature Amplitude Modulation
QPSK	Quaternary Phase Shift Keying

RF	Radio-Frequency
SNR	Signal to Noise Ratio
THz	Terahertz

1. INTRODUCTION

1.1. Evolution of Wireless Communications

Wireless communications have advanced significantly since the introduction of the first generation. Emerging trends and technologies have shaped, and continue to shape, the standards for future wireless generations. In particular, the proliferation of smartphones has accelerated the demand for integrating new technologies into wireless communications. Institutions such as the ITU and 3GPP have proposed guidelines and recommendations for newer wireless generations to address these evolving demands. For example, the IMT-2020 report emphasized the need for enhanced mobile broadband, massive machine-type communications, and ultra-reliable low-latency communications.

Since the release of IMT-2020 report, new trends and technologies have emerged. Additionally, the COVID-19 pandemic has led to a rapid increase in new online multimedia applications, significantly raising the importance of low-latency mobile communication services. 5G mobile networks experienced a 40% increase in data traffic between 2021 and 2022 (Weissberger, 2022), primarily driven by a growing number of smartphone subscriptions and increased video content consumption following the pandemic.

In response to these developments, the IMT-2030 report expanded on use cases and standards outlined in the previous report. The report ends by recommending a peak data rate greater than 50 Gbit/s. This is a reasonable expectation, as the minimum data-transmission requirement for holographic communication has been determined to be in the tens of Gbit/s (Xu et al., 2011).

The recommendation of more than 50 Gbit/s implies the use of bandwidths on the order of tens of GHz. Given the high congestion and strict regulations in the lower portions of the mm-wave

spectrum, these bands are unlikely to satisfy this new requirement. Thus, the report also considers using spectrum above 92 GHz in addition to lower bands. This motivates research and development of wireless-communication links operating in the sub-THz range. In the literature, 100 GHz is considered to be the lower bound of the sub-THz band (Heydari, 2021). Implementing a transmitter in these bands presents both inherent advantages and challenges, which will be discussed next.

1.2. Some Considerations of Implementing a Transmitter in sub-THz bands

The higher portions of the mm-wave spectrum, especially the sub-THz bands, are largely unused; thus, the congestion is very low. These bands can still deliver high data rates even when spectrally inefficient, low-order modulation schemes and small fractional bandwidths are used. For example, an on–off keying (OOK) signal centered at 100 GHz with a 10 % fractional bandwidth can support 10 Gbit/**s** throughput. At sub-THz frequencies, a 10 % fractional bandwidth can reasonably be achieved with standard silicon technologies (Heydari, 2021). In addition, antennas and other passive components shrink in size, reducing on-chip area and enabling the integration of multiple antennas on a chip without excessive packaging or interconnects (Kang et al., 2015).

However, implementing transmitters in the sub-THz bands presents several difficulties. The main challenge is the huge path loss of electromagnetic waves at these high carrier frequencies (Pozar, 2011). In sub-THz links, this path loss leads to a significant reduction in received power, which lowers the receiver's sensitivity and limits the communication range to on the order of centimeters. The problem can be mitigated on the transmitter side with high-output-power amplifiers. Unfortunately, standard CMOS power amplifiers in the sub-THz range suffer from relatively low f_{max}, the frequency of unity power gain. This limitation has motivated the development of amplifiers based on III-V technologies, whose transistors offer much higher f_{max} values, as illustrated in Fig. 1. However, these III-V solutions reportedly provide low yield and limited integrability, hindering their scalability in sub-THz transmitters (Banerjee, 2024).

Heydari (2021) establishes an intuitive upper bound of $f_{max}/2$ for transistors, above this limit they no longer deliver sufficient gain or output power while maintaining acceptable power-added

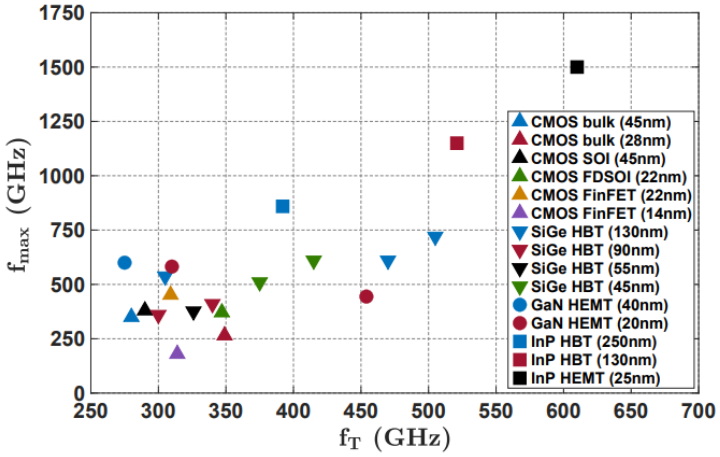

Figure 1: f_{max} of several semiconductor technologies. Reprinted from "Sub-THz Integrated Circuits: Challenges and Opportunities," by A. Banerjee, 2024, *Proceedings of the 2024 IEEE 67th International Midwest Symposium on Circuits and Systems (MWSCAS)* (pp. 764–768), IEEE. © 2024 IEEE.

efficiency. It can be inferred from Figure 1 that the sub-THz frequency range over which bulk CMOS power amplifiers remain viable is rather narrow. Consequently, conventional transmitter architecture described by Badal (2019), which relies on IQ modulation and uses a CMOS amplifier in the final stage, may have limited applicability at sub-THz frequencies. An example of this architecture is shown in Figure 2.

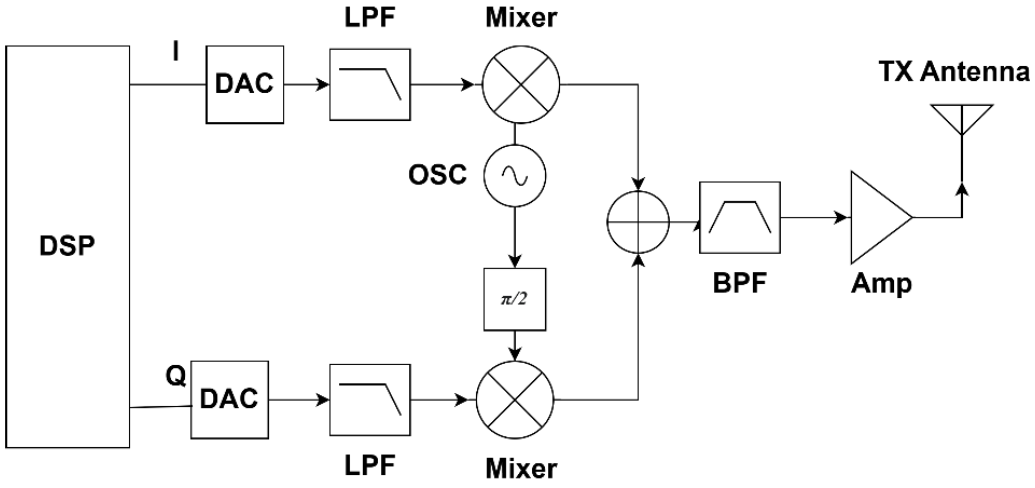

Figure 2: PA-last RF transmitter (conventional)

In this transmitter architecture:

1. The DSP block generates the I and Q data streams and performs the necessary filtering operations, such as pulse-shaping.
2. In each branch**,** a DAC converts the digital data to its analog equivalent. An LPF may be required to suppress the high-frequency artifacts introduced by up-sampling.
3. Mixers upconvert the signals to the intended frequency band.
4. A power combiner sums the upconverted analog I and Q waveforms.
5. A BPF may be needed to suppress the image components generated by the mixer.
6. The power amplifier compensates for the mixer conversion loss and delivers sufficient power output. Finally, the signal is radiated by the antenna.

Several sub-THz transceivers in the literature (D'heer & Reynaert, 2024; Eissa et al., 2018; Fujishima, 2013; Rodríguez-Vázquez et al., 2018, 2019, 2020; Sarmah et al., 2016; Tokgöz et al., 2018; Tokgöz & Okada, 2019; Wang et al., 2014) employ transmitter topologies similar to the one shown in Figure 2. Most of them, however, use amplifiers based on III-V technologies. These implementations show that the communication range can be extended to over tens of meters by utilizing both a high-gain amplifier and a lens antenna.

On the other hand, there have been efforts to investigate alternative transmitter architectures aiming to overcome the f_{max} limitation. One approach adds a passive mixer stage (Abdo et al., 2020, 2022; Güngör & Reynaert, 2024; Katayama et al., 2016; Lee et al., 2019, 2024; Takano et al., 2017) after the amplifier to upconvert the signal to the sub-THz band. Such architectures suffer from low output power because of the conversion loss of passive mixers. The resulting loss increases the link budget and leads to a nonnegligible EVM which scales inversely with the SNR of the signal (Gharaibeh et al., 2004).

Another architecture proposed to overcome the f_{max} limitation employs a frequency multiplier in the final stage (Darwish et al., 2016; Kang et al., 2015; Standaert & Reynaert, 2020; Thomas et al., 2024). The nonlinear characteristics of multipliers inherently provide frequency upconversion by

generating the signal's harmonics. However, this architecture suffers from low output power because of the conversion loss of the multiplier, although the loss is more moderate than in mixer-last transmitters. In addition, multiplier nonlinearity severely degrades the modulated waveform with respect to SNR and EVM and causes bandwidth expansion, which in turn adversely affects ACPR. Consequently, frequency-multiplier-last transmitters are generally limited to low order, spectrally inefficient digital modulations unless a suitable mitigation technique is employed.

Table 1 compares published sub-THz transceivers that implement the three transmitter architectures previously mentioned. The table also serves as a concise summary of the discussion presented in the Introduction section.

Table 1: Performance Comparison of Several Sub-THz Transceivers

	(Vasquez et al., 2018)	(Eissa et al., 2018)	(Katayama et al., 2016)	(Lee et al., 2018)	(Kang et al., 2015)	(Thomas et al., 2024)
Technology	13nm SiGe	SiGe BiCMOS	40nm CMOS	40nm CMOS	65nm CMOS	90nm SiGe BiCMOS
Last-stage component	Amplifier	Amplifier	Mixer	Mixer	Tripler	Quadrupler
Center frequency (GHz)	240	240	300	248	240	398
3-dB Bandwidth (GHz)	35	35	-	-	10.7	30
P_{out} (dBm)	8.5	-5	-14.5	-17.2	0	-9.4
Modulation	BPSK	BPSK	32-QAM	32-QAM	QPSK	OOK
Data rate (Gbps)	25	20	17.5	10	10	2
Signal Quality	7% EVM	BER $< 10^{-6}$	6.7% EVM	11.5% EVM	BER $< 10^{-6}$	BER $< 10^{-6}$
Communication range	100 cm	15 cm	-	-	2cm	20cm

1.3. Motivation and Organization of the Thesis

Multiplier-last transmitters enable sub-THz communication using solely CMOS technology.

However, they significantly suffer from degraded modulation characteristics of the transmitted signals. Given the limited research on how frequency multipliers affect digital communication performance, a comprehensive system-level analysis could contribute to the research on frequency-multiplier-last transmitters. The remainder of the thesis is structured as follows: Chapter 2 provides the theoretical background on IQ modulation, which is widely adopted in digital communications, and modeling the nonlinearity of frequency multipliers. Chapter 3 reviews the literature on frequency-multiplier-last transmitters and techniques for compensating distortions introduced by multipliers. Chapter 4 introduces a model for analyzing impairments caused by frequency multipliers and applies it to evaluate SNR degradation and constellation distortion. Finally, Chapter 5 presents conclusions and discusses potential future research directions regarding multiplier-last transmitters.

2. Background

2.1 IQ Modulation and Constellation Diagram

Wireless systems often employ in-phase and quadrature (I/Q) modulation to increase spectral efficiency, transmitting more bits per unit time. IQ modulation exploits the trigonometric identities of sine and cosine waves, enabling independent detection of each data in I/Q branches.

Consider the transmitter scheme shown in Figure 2. It consists of two separate branches: one mixer multiplies the signal with a cosine wave in the I branch, while the other mixer multiplies it with a sine wave in the Q branch. Let the I and Q data as V_I and V_Q; the resulting IQ-modulated signal is expressed in (2.1).

$$s(t) = V_I cos(wt) + V_Q sin(wt) \tag{2.1}$$

As shown in Figure 3, the demodulator at the receiver downconverts the signal to baseband using a mixer. Next, an LPF removes unwanted frequency components, leaving only the baseband component. Any amplitude scaling introduced by the mixer can be compensated for by adjusting the LPF gain. The process in each branch can be illustrated as follows.

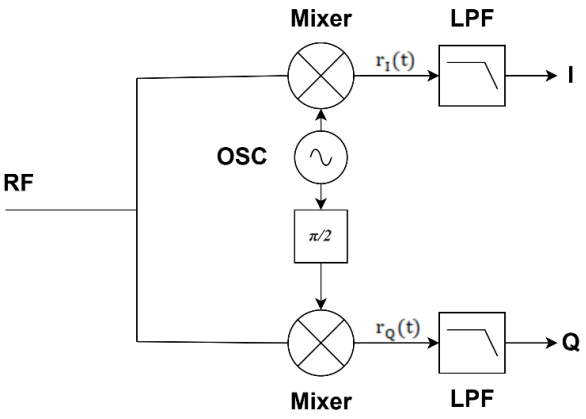

Figure 3: IQ demodulator in the receiver

$$r_I(t) = \big(V_I cos(wt) + V_Q sin(wt)\big)cos(wt) = \frac{V_I}{2}cos(2wt) + \frac{V_Q}{2}sin(2wt) + \frac{V_I}{2} \quad (2.2)$$

$$r_Q(t) = \big(V_I cos(wt) + V_Q sin(wt)\big)sin(wt) = \frac{V_I}{2}sin(2wt) - \frac{V_Q}{2}cos(2wt) + \frac{V_Q}{2} \quad (2.3)$$

Applying a low-pass filter with a cutoff frequency below 2ω removes the unwanted sinusoidal components, isolating the I- and Q-signals in their respective branches. Setting the LPF gain to 2 restores the amplitudes of both I and Q signals.

Digital modulations such as M-PSK and M-QAM can be implemented using IQ modulation. For example, QPSK (4-PSK) modulation is formed by letting $V_I = \{\frac{-1}{\sqrt{2}}, \frac{1}{\sqrt{2}}\}$ and $V_Q = \{\frac{-1}{\sqrt{2}}, \frac{1}{\sqrt{2}}\}$, as shown in Table 2.

Table 2: Forming QPSK by IQ Modulation

Symbol	**Amplitude of V_I**	**Amplitude of V_Q**	**Phase of QPSK**
S_{11}	$\frac{1}{\sqrt{2}}$	$\frac{1}{\sqrt{2}}$	$\frac{\pi}{4}$
S_{12}	$\frac{-1}{\sqrt{2}}$	$\frac{1}{\sqrt{2}}$	$\frac{3\pi}{4}$
S_{21}	$\frac{1}{\sqrt{2}}$	$\frac{-1}{\sqrt{2}}$	$\frac{5\pi}{4}$
S_{22}	$\frac{-1}{\sqrt{2}}$	$\frac{-1}{\sqrt{2}}$	$\frac{7\pi}{4}$

Constellation diagrams provide a two-dimensional representation of digital modulation schemes based on their I and Q components. Because sine and cosine waves are orthogonal, each wave can be assigned to orthogonal axes in the 2D plane. For example, the QPSK values listed in Table 2 can be visualized in the constellation diagram shown in Figure 4. Similarly, other PSK and QAM schemes can be represented similarly.

The IQ-modulated and upconverted signals also admit a complex passband representation, given in (2.4), which characterizes the waveform solely through its I and Q components.

$$s(t) = Re\{(V_I + jV_Q)e^{jw_c t}\} = V_I cos(wt) - V_Q sin(wt) \quad (2.4)$$

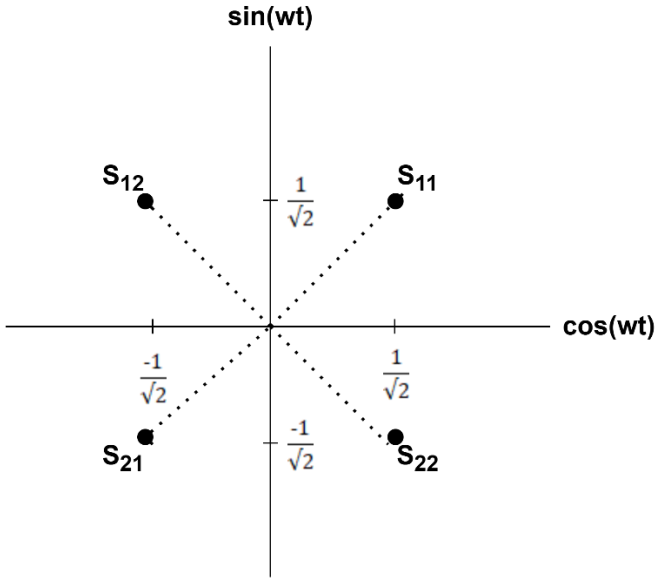

Figure 4: Constellation diagram of QPSK modulation

2.2 Modeling of Frequency Multipliers

As a nonlinear device, a frequency multiplier is an integral component of wireless systems, particularly for shifting the local-oscillator (LO) signal from a lower to a higher frequency. This shift is accomplished by exploiting the multiplier's nonlinearity to generate harmonics and selecting the desired harmonic with a BPF. Carrier waves in the mm-wave and sub-THz bands can thus be generated, as shown in Figure 5.

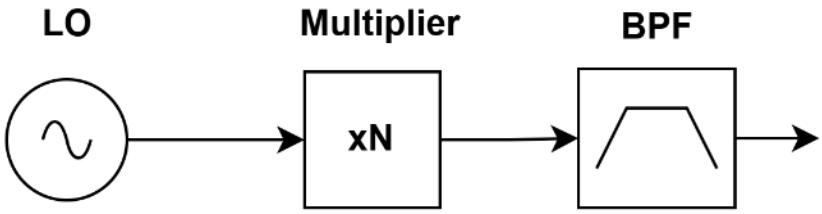

Figure 5: High-frequency carrier wave generation

Because frequency multipliers are nonlinear devices, their behavior can be modeled by a power-series expansion of their input signal. Consequently, the output of the frequency multiplier can be expressed as:

$$y(t) = \sum_{n=1}^{N} c_n x^n(t) \tag{2.5}$$

where c_n denotes a set of constant coefficients. (2.5) explains how carrier waves are upconverted to higher frequencies. If x(t) is a sinusoid, i.e., x(t)=Acos(ωt) with constant amplitude A, then applying a frequency multiplier of order N generates harmonics of the input signal, from the fundamental at frequency f to the Nth harmonic at Nf. For example, a frequency tripler (N=3) produces the following harmonics of x(t):

$$y(t) \; = \; c_1 x(t) \; + \; c_2 x^2(t) \; + c_3 x^3(t)$$

$$y(t) = \frac{c_2 A^2}{2} + \left(c_1 A + \frac{3c_3 A^3}{4} \right) cos(wt) + \frac{c_2 A^2}{2} cos(2wt) + \frac{c_3 A^3}{4} cos(3wt) \tag{2.6}$$

A BPF centered at 3f suppresses all unintended harmonics in (2.6), isolating the third harmonic. Assuming the BPF has unity gain, the signal after the filter becomes

$$s(t) = \frac{c_3 A^3}{4} cos(3wt) \tag{2.7}$$

By comparing s(t) with x(t), we see that the amplitude of the carrier wave x(t) is multiplied by three, a phenomenon known as AM–AM distortion. Likewise, a sinusoid with phase θ is converted to one with phase 3θ by a frequency tripler; this effect is called PM–PM distortion. This behaviour is problematic when the local-oscillator (LO) already contains phase noise. A frequency multiplier of order N increases the phase noise by roughly 10log(N) dB (Camargo, 2017). Therefore, the multiplier unintentionally alters both the amplitude and phase of modulated signals, compromising the quality of digital communication.

3. Literature Review

In the literature, research on frequency-multiplier-last transmitters for digitally modulated wireless systems falls into two main areas: (1) digital predistortion techniques to compensate for the impairments introduced by frequency multipliers, and (2) system-level implementations of frequency-multiplier-last transmitters.

3.1. Digital Predistortion of Frequency Multipliers

As with power amplifiers, frequency multipliers can be linearized by applying a digital predistortion (DPD) module. The key difference is that the desired output is not a linearly amplified version of x(t), but rather $x^N(t)$, so that frequency upconversion is achieved according to the multiplier order N. Consequently, the nonlinearity and memory effects that cause AM-AM and AM-PM distortions must still be corrected.

Liu et al. (2016) presents a clear framework for linearizing a frequency multiplier: it examines a frequency quadrupler and gives the Volterra-series model and its inverse in (3.1) and (3.2).

$$y(n) = \sum_{m_1=0}^{M_1-1} \sum_{m_2=0}^{M_2-1} \sum_{k=1}^{K_q} b_{m_1 m_2 k} x^4(n-m_1) |x(n-m_2)|^{k-1} \tag{3.1}$$

$$x^4(n) = \sum_{m_1=0}^{M_1-1} \sum_{m_2=0}^{M_2-1} \sum_{k=1}^{K_q} c_{m_1 m_2 k} y(n-m_1) |y(n-m_2)|^{k-1} \tag{3.2}$$

An estimate of $c_{m_1 m_2 k}$ is obtained through a least-squares solution, denoted $\bar{\mathrm{c}}_{\mathrm{m_1 m_2 k}}$. These estimated coefficients replace those in (3.1) to produce a predistorted signal, which is then expected to linearize the output of the frequency quadrupler. However, unlike power amplifiers, frequency multipliers impose bandwidth expansion on the signal, proportional to the multiplier order. Therefore, a Dth-root module, which computes the Dth root of the predistorted signal, is typically inserted after the DPD block in baseband (e.g., Liu et al. (2016), Jaffri et al. (2020), Tripathi & Rawat (2023)) to counteract this expansion.

Once the signal passes through the frequency multiplier of order N, its bandwidth is effectively restored to that of the original waveform. It is also essential to unwrap the phase of the predistorted signal to prevent phase jumps after the frequency multiplier. These steps are essential to the digital predistortion procedure that precedes the multiplier.

The resulting predistorted signal is then fed into a DAC, upconverted by an intermediate mixer stage, amplified by a driver, and passed through the frequency quadrupler. Figures 6 and 7 illustrate the linearized AM–AM and AM–PM characteristics and the compensation for bandwidth expansion.

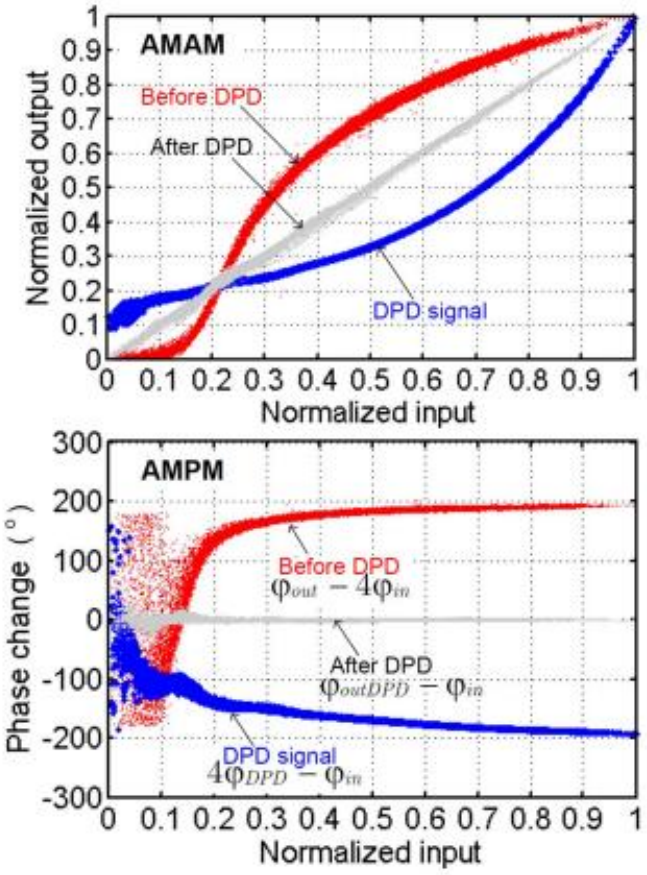

Figure 6: Linearized AM–AM and AM–PM curves of a frequency quadrupler. Reprinted from "High-order modulation transmission through frequency quadrupler using digital predistortion," by Y. Liu, G. Liu, and P. M. Asbeck, 2016, *IEEE Transactions on Microwave Theory and Techniques, 64*(6), 1896–1910. © 2016 IEEE.

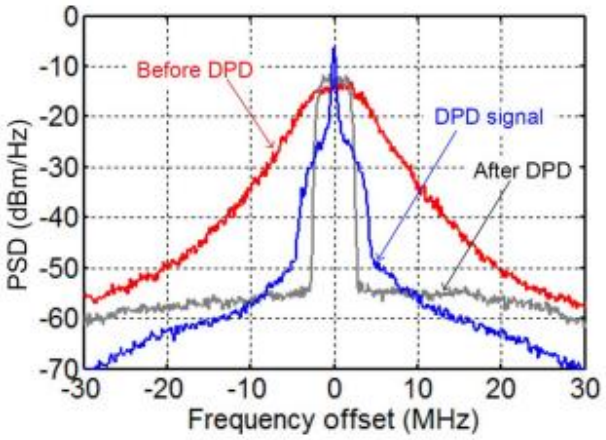

Figure 7: Compensated bandwidth expansion by DPD. Reprinted from "High-order modulation transmission through frequency quadrupler using digital predistortion," by Y. Liu, G. Liu, and P. M. Asbeck, 2016, *IEEE Transactions on Microwave Theory and Techniques, 64*(6), 1896–1910. © 2016 IEEE.

Residual nonlinearities at low input power levels may persist in the AM–PM curve even after applying DPD. To address this, Liu et al. (2016) proposed cascading two DPD modules, which improved linearization for 5 MHz, 10 MHz, and 20 MHz 256-QAM test signals. In particular, the EVM was reduced from 140 % to 2 %, and the ACPR improved to −40 dBc. The maximum data rate reported was 138.24 Mbit/s for a 20 MHz 256-QAM signal. However, the computational complexity of DPD for frequency multipliers remains higher than that for power amplifiers. The bandwidth of the modulated signal also tends to be relatively low.

Nopchinda et al. (2018) reduced computational complexity by predistorting only the phase of an 8-PSK signal. This approach increased the data rate to 4.8 Gbit/**s**, albeit at the cost of higher BER (2×10^{-4}) and EVM (9.8 %). On the other hand, this phase-only method is valid only for phase-modulated signals. Meanwhile, Jaffri et al. (2020) showed the number of coefficients in (3.1) and (3.2) can be significantly pruned while maintaining linearization performance, based on two key observations:

1. Nonlinear terms beyond the multiplier order minimally affect distortion.
2. Adding delay terms beyond the Nyquist rate of the multiplier output also has a minor impact on distortion.

By pruning these terms, the DPD complexity can be kept in check while supporting wider signal bandwidths, e.g., up to 800 MHz in Jaffri et al. (2020), without excessive computational overhead.

Nevertheless, DPD is designed specifically to correct the frequency multiplier's nonlinearity, assuming that other transmitter components operate ideally and do not undermine its performance. Moreover, the iterative algorithms used to estimate DPD coefficients, such as least-squares solvers, can sometimes fail to converge, leading to divergence in specific scenarios.

3.2.Frequency-Multiplier-Last Transmitters

The literature is scarce with system-level implementations of frequency-multiplier-last transmitters. Kang et al. (2015) reported the first CMOS-based sub-THz transmitter that employs this architecture. The system block diagram is shown in Figure 8. The transmitter operates at 240 GHz with a 10.7 GHz 3-dB bandwidth and supports both BPSK and QPSK modulation schemes.

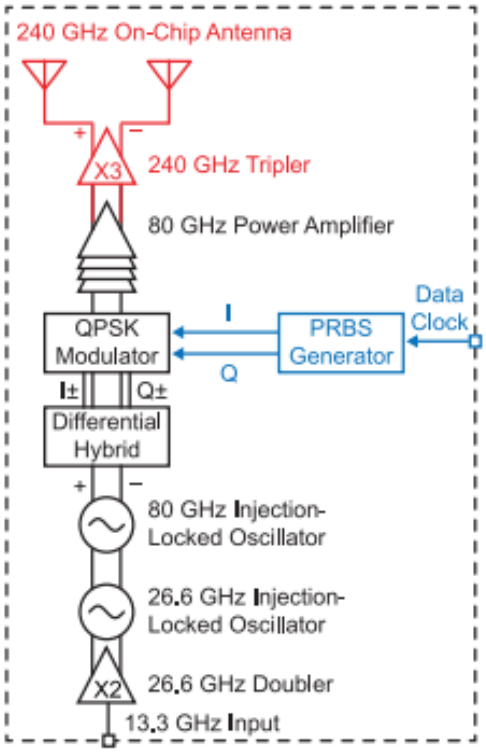

Figure 8: System architecture. Reprinted from “A 240 GHz fully integrated wideband QPSK transmitter in 65 nm CMOS,” by S. Kang, S. V. Thyagarajan, and A. M. Niknejad, 2015, *IEEE Journal of Solid-State Circuits, 50*(10), 2256–2267. © 2015 IEEE.

An 80 GHz carrier is generated from a 13.3 GHz LO input, which is doubled to 26.6 GHz and then phase-locked to 80 GHz. The system uses I/Q modulation: a differential hybrid splits the carrier into cosine and sine components, forming the I and Q branches. Two pseudo-random binary sequence (PRBS) generators, each running at 4 Gbit/s, supply data to the I and Q mixers, creating two independent streams. A QPSK modulator multiplies these I and Q signals by their respective carriers and then sums them differentially. Afterward, a power amplifier boosts the 80 GHz signal, which is upconverted to 240 GHz by a frequency-tripler. The 240 GHz antenna, with a 30 GHz bandwidth, inherently suppresses the lower-order harmonics at 80 GHz and 160 GHz.

Measurements show a maximum data rate of 16 Gbit/s with the receiver placed 2 cm from the transmitter. The received signal is downconverted to baseband by a sub-harmonic mixer, and its spectrum is captured on a spectrum analyzer as shown in Figure 9. The QPSK signal is sampled at 8 GS/s, achieving a 16 Gbit/s data rate. A null at 8 GHz in the spectrum indicates a sinc-shaped envelope, confirming that the rectangular PRBS pulses were not pulse-shaped; consequently, no bandwidth expansion appears in the null-to-null bandwidth. Thus, it can be inferred that no pulse shaping was applied in this transmitter.

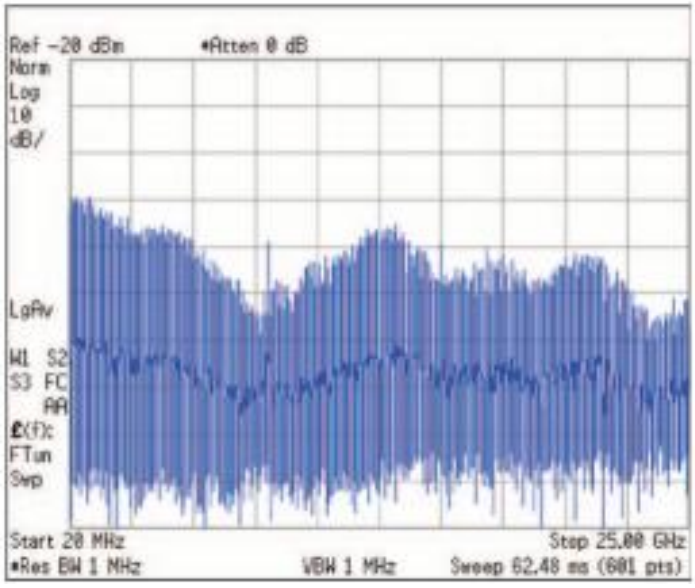

Figure 9: Spectrum of 8GSps modulated signal. Reprinted from “A 240 GHz fully integrated wideband QPSK transmitter in 65 nm CMOS,” by S. Kang, S. V. Thyagarajan, and A. M. Niknejad, 2015, *IEEE Journal of Solid-State Circuits, 50*(10), 2256–2267. © 2015 IEEE.

However, signal integrity becomes a concern when a frequency multiplier is applied to a QPSK signal. Intuitively, one would expect the output signal's phase to be distorted, causing the constellation points to deviate from their ideal positions. As shown in the next section, QPSK signals can indeed preserve the constellation points at the output of the frequency tripler, but they become permuted. Consequently, a conventional detection process that relies on predefined decision regions may misinterpret symbol locations and thereby inflate the bit-error rate (BER). Kang et al. (2015) did not address this issue.

Darwish et al. (2016), and Standaert and Reynaert (2020) adopted an outphasing technique, illustrated in Fig. 10, which offers an alternative modulation method and potential distortion mitigation.

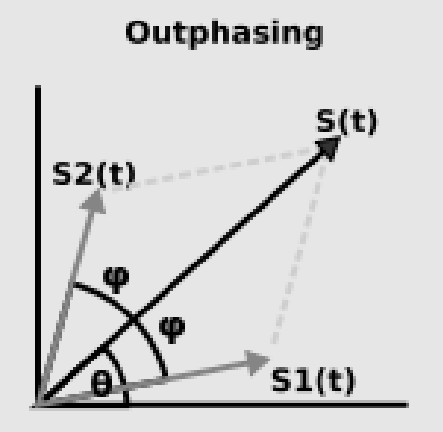

Figure 10: Outphasing method. Reprinted from "A 390-GHz outphasing transmitter in 28-nm CMOS," by A. Standaert and P. Reynaert, 2020, *IEEE Journal of Solid-State Circuits, 55*(10), 2703–2713. © 2020 IEEE.

In this technique, the in-phase and quadrature signals are generated by cascading a phase shifter with a frequency multiplier, allowing direct modulation of the carrier's amplitude and phase. A power combiner subsequently sums the resulting signals, $S_1(t)$ and $S_2(t)$, as shown in Figure 10. The implementation presented in Darwish et al. (2016) is illustrated in Figure 11. Transmitter design shown in Figure 11 employs both BPSK and 16-QAM modulation schemes. In each branch, a 24th-order frequency multiplier modulates the phase of the carrier wave. A power amplifier operating near saturation region boosts the signal power at the multiplier output, degrading the modulation quality. The measured EVM for 16-QAM is 5.7 %. The modulation quality of this

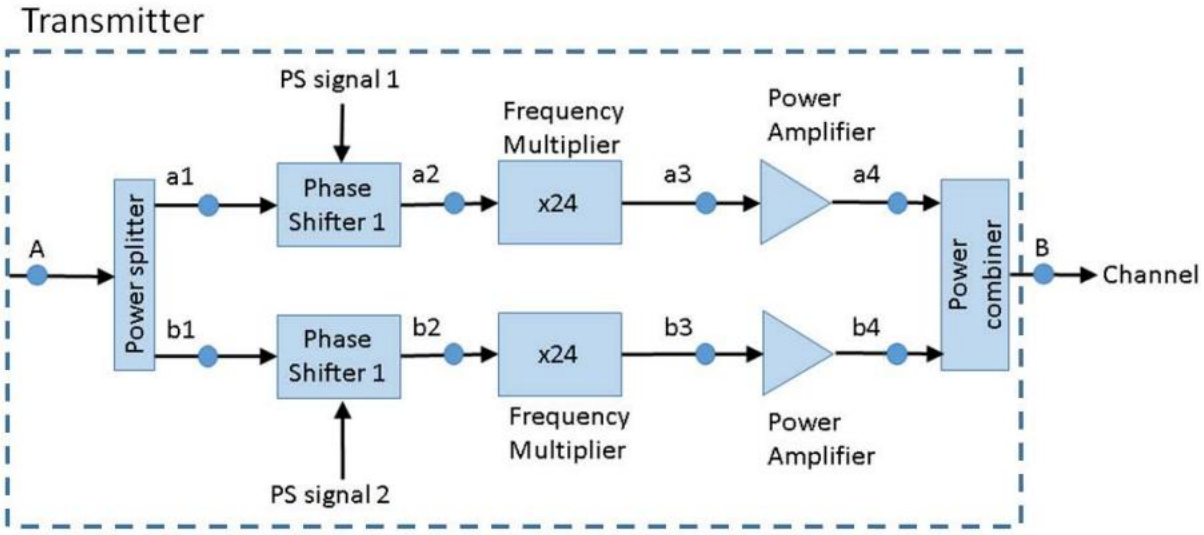

Figure 11: Outphasing implementation. Reprinted from "Efficient linear transmission of complex waveforms at 216 GHz using nonlinear multiplier chains," by A. Darwish, J. Qiu, E. Viveiros, H. A. Hung, and J. Hesler, 2016, *Proceedings of the IEEE MTT-S International Microwave Symposium Digest (IMS)*, San Francisco, CA, USA, May 2016. © 2016 IEEE.

architecture is also susceptible to the mismatch between the two branches. Standaert and Reynaert (2020) used an outphasing symbol generator which creates two phase-modulated signals $S_1(t)$ and $S_2(t)$ at a low-frequency carrier. Each signal is then upconverted using a high-frequency local oscillator, amplified, and tripled. After the tripling process, the two signal paths are recombined at the output coupler. The phase modulator uses 5 bits from the symbol generator to encode the amplitude (3 bits) independently and the phase (2 bits) of the low frequency carrier utilizing a DLL (Delay Locked Loop). This configuration achieves a maximum data rate of 6 Gbps but suffers from relatively high EVM and low output power, making it less practical for real wireless systems. Measurements were conducted using a waveguide flange for evaluation.

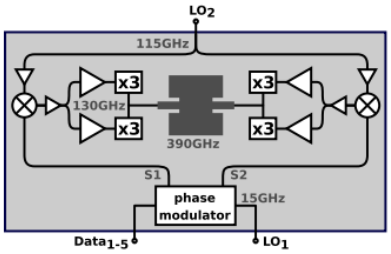

Figure 12: Block diagram of outphasing transmitter. Reprinted from "A 390-GHz outphasing transmitter in 28-nm CMOS," by A. Standaert and P. Reynaert, 2020, *IEEE Journal of Solid-State Circuits, 55*(10), 2703–2713. © 2020 IEEE.

Thomas et al. (2024) presented another implementation of a frequency-multiplier-last transmitter that uses a reverse-recovered silicon p-i-n diode as a frequency quadrupler. In this design, a 100 GHz LO signal undergoes OOK modulation and is then upconverted to 400 GHz by the quadrupler. Since OOK detection depends only on the presence or absence of the carrier, it is inherently immune to the amplitude and phase distortion introduced by the frequency multiplier. However, it is not immune to bandwidth expansion contrary to the claim made in the paper's Appendix. Because, squaring the product of a wide-band signal and a carrier always yields a term proportional to the square of the signal, which broadens its bandwidth if the signal has finite bandwidth.

From a system-level perspective, several challenges remain when implementing frequency-multiplier-last transmitters for sub-THz wireless links. First**,** output power levels are low due to conversion loss by the multiplier, severely limiting communication range. Second**,** the multiplier's amplitude and phase distortion make it difficult to use spectrally efficient, higher-order modulations. To obtain a fully functional multiplier-last transmitter, a DPD module is required, with the cost of more power consumption and overall system complexity.

4. ANALYSIS OF IMPAIRMENTS OF FREQUENCY MULTIPLIERS

The first three sections showed that frequency multipliers can severely degrade the modulation characteristics and cause bandwidth expansion. However, little effort has been made to quantify the impact of a frequency multiplier on digital communications as a function of its nonlinearity. Liu et al. (2016) reported an SNR degradation of approximately 12 dB after a quadrupler, attributed to an elevated noise floor caused by mixing between the signal and noise components. In the work of Chung et al. (2019), the input-noise power is shown to experience a gain of $10 \log_{10} N$, where N is the multiplier order.

This section presents a generalized derivation of SNR degradation and constellation distortion induced by an N-fold multiplier. The analysis is based on the communication-chain model in Figure 13. Data from the I and Q branches are first pulse shaped and IQ-modulated. The AWGN is then added, and a BPF suppresses the image components generated by the upconversion mixing stage. After the N-fold multiplier, a second bandpass filter suppresses all harmonics except the Nth, isolating the desired harmonic at the multiplier output.

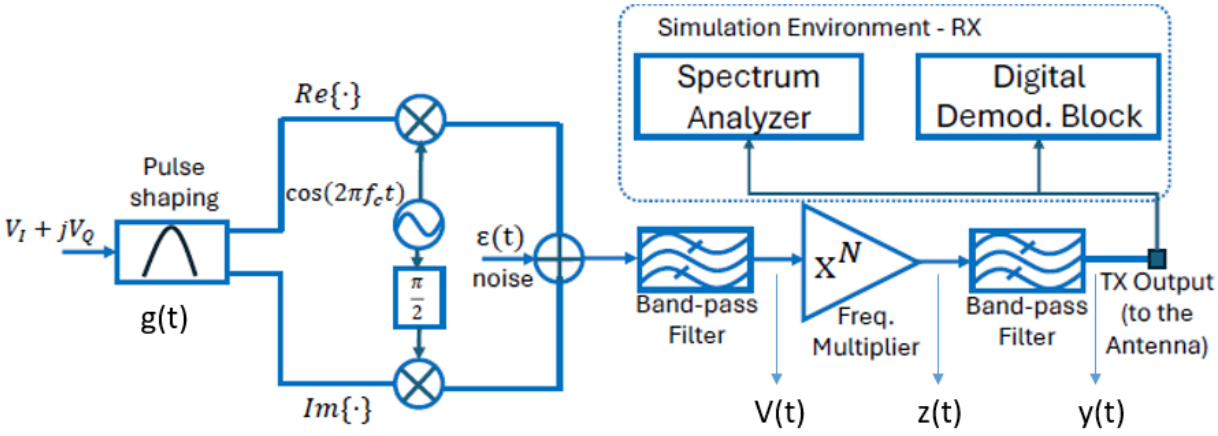

Figure 13: A system model for communication chain of frequency multipliers

Noise, denoted by ε(t), is included only in the calculation of SNR degradation at the output of the frequency multiplier. It will be shown that the multiplier's nonlinearity alone can impair the unambiguous detection of modulated signals in specific scenarios, even when no noise is present.

4.1. Bandwidth Expansion

In the previous sections, bandwidth expansion was shown to arise from the wideband spectrum of the PRBS data, whereas the carrier merely translates the spectrum in frequency. Therefore, examining the frequency response of the Nth power of bit pulses at baseband is sufficient.

$$h(t) = m^N(t) \tag{4.1}$$

Interestingly, when no pulse shaping is applied and the bits are transmitted as rectangular pulses, their bandwidth remains unchanged after passing through any frequency multiplier, since

$$\Pi\left(\frac{t}{T_b}\right)^N = \Pi\left(\frac{t}{T_b}\right) \tag{4.2}$$

Therefore, in terms of all three bandwidth definitions, absolute, null-to-null, and essential, the bandwidth remains unchanged because the pulse does not change. The absolute bandwidth is still infinite; the null-to-null bandwidth is $2T_b$; and the essential bandwidth is approximately equal to the null-to-null bandwidth. These results are verified in the frequency domain, as shown in Figure 14, where nonlinearity in the time domain corresponds to convolution in the frequency domain. This also explains why no bandwidth expansion is observed in the work of Kang et al. (2015).

The conclusion can be further confirmed by examining the magnitudes of the truncated harmonics in the Fourier series expansion of an infinite pulse train when the signal is subjected to third order nonlinearity. As the number of retained harmonics increases, the magnitudes after tripling approach those of the original signal. For example, the magnitude of the first harmonic in Figure 16 is 0.6366; for N=3 it becomes 0.688; for N=5**,** 0.664; for N=7**,** 0.6538; and for N=9**,** 0.6485. Thus, as additional harmonics are included, the magnitude of the first harmonic converges toward its original value of 0.6366.

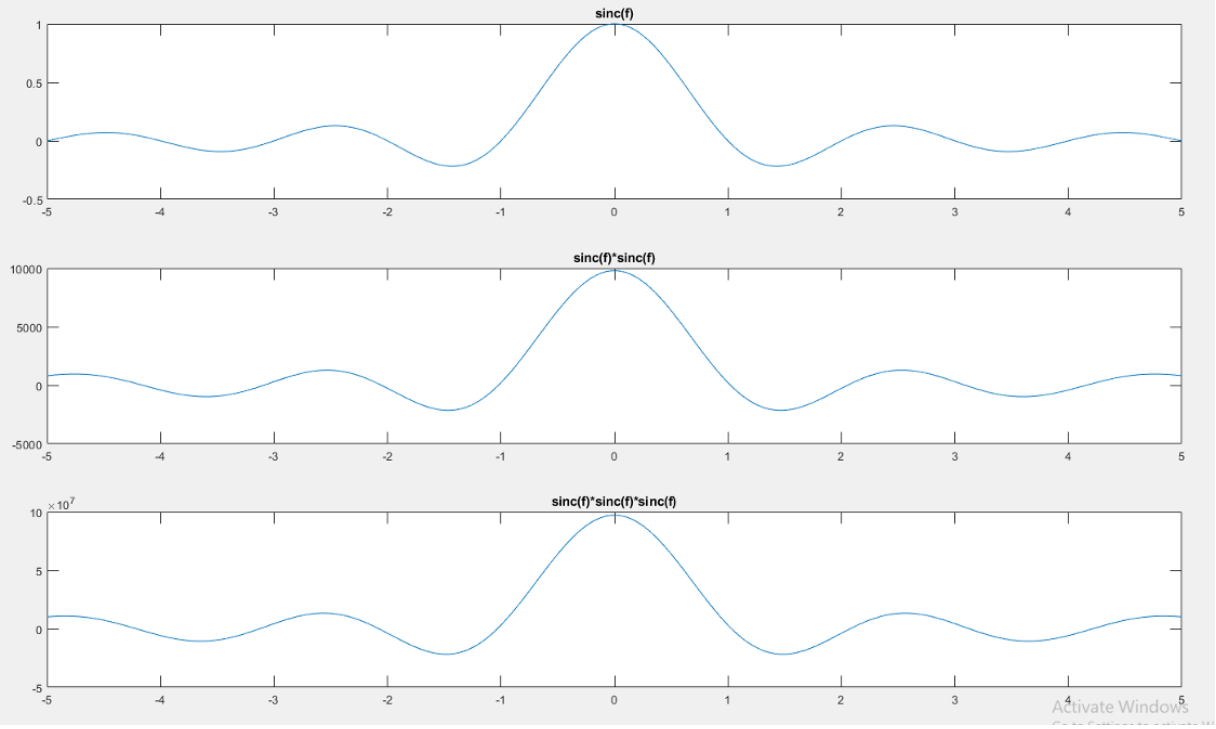

Figure 14: The change of spectrum of sinc pulse after nonlinearity

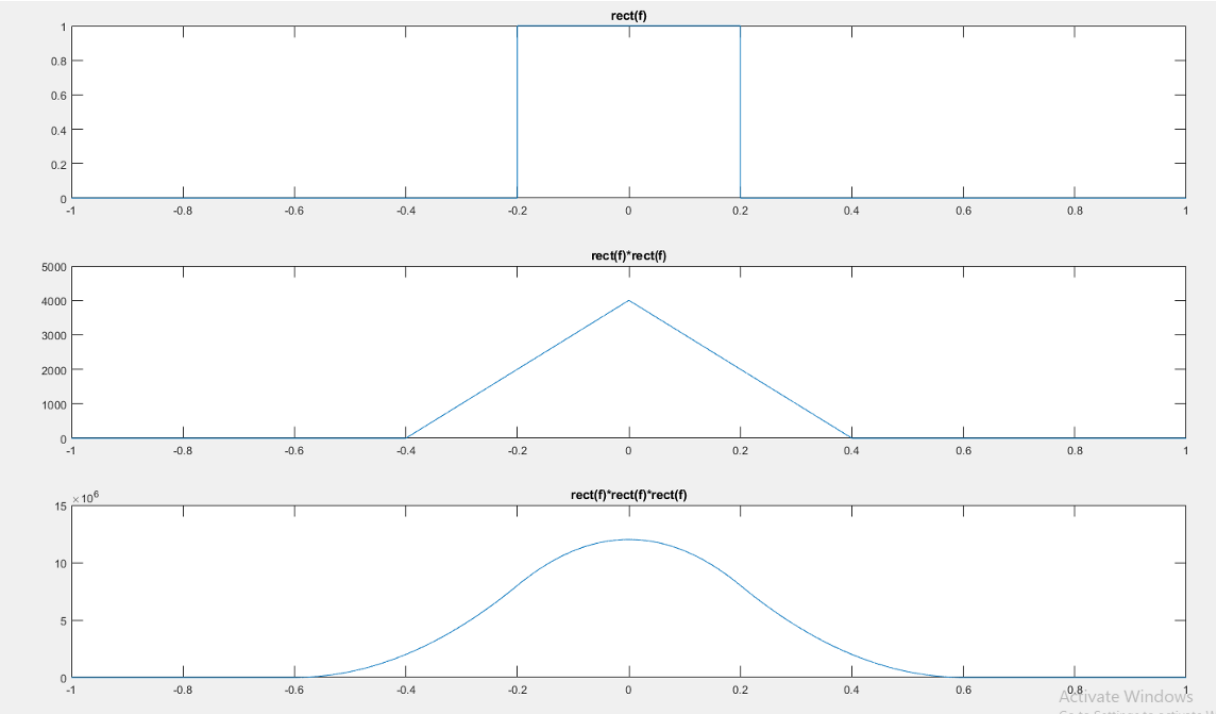

Figure 15: The change of spectrum of the rect pulse after nonlinearity

N=3

$$x(t) = \sum_{k=-3}^{3} \frac{2}{j\pi k} e^{j2\pi k f_0 t}$$

k	Magnitude before tripling	Magnitudes after tripling	Products that Falls in kth Harmonic
-9	-	0.0095	D_{-3}^3
-7	-	0.086	$3D_{-3}^2 D_{-1}$
-5	-	0.172	$3D_{-3}^2 D_1$, $3D_{-1}^2 D_3$
-3	0.21222	0.2867	$3D_{-3}^2 D_3$, $6D_{-3} D_{-1} D_1$, D_{-1}^3
-1	0.6366	0.6880	$3D_{-1}^2 D_1$, $6D_{-3} D_{-1} D_3$, $3D_{-1}^2 D_1$
1	0.6366	0.6880	$3D_{-1}^2 D_3$, $6D_{-3} D_1 D_3$, $3D_1^2 D_3$
3	0.2122	0.2867	$3D_3^2 D_{-3}$, $6D_{-1} D_1 D_3$, D_1^3
5	-	0.172	$3D_1^2 D_3$, $3D_3^2 D_{-1}$
7	-	0.086	$3D_3^2 D_1$
9	-	0.0095	D_3^3

Figure 16: The change of amplitudes after tripling when the number of harmonics is 3

N=5

$$x(t) = \sum_{k=-5}^{5} \frac{2}{j\pi k} e^{j2\pi k f_0 t}$$

```
harmonics = [-2/(pi*1i*5) -2/(pi*1i*3) -2/(pi*1i) 2/(
   pi*1i) 2/(3*pi*1i) 2/(5*pi*1i)];

conv(conv(harmonics,harmonics),harmonics);
```

k	Magnitudes before tripling	Magnitudes after tripling
-15	-	0.0021
-13	-	0.0103
-11	-	0.0482
-9	-	0.0818
-7	-	0.1273
-5	0.1273	0.1782
-3	0.2122	0.2557
-1	0.6366	0.6640
1	0.6366	0.6640
3	0.2122	0.2557
5	0.1273	0.1782
7	-	0.1273
9	-	0.0818
11	-	0.0482
13	-	0.0103
15	-	0.0021

Figure 17: The change of amplitudes after tripling when the number of harmonics is 5

N=9

$$x(t) = \sum_{k=-9}^{9} \frac{2}{j\pi k} e^{j2\pi k f_0 t}$$

```
harmonics = [-2/(pi*1i*9) -2/(pi*1i*7) -2/(pi*1i*5)
   -2/(pi*1i*3) -2/(pi*1i) 2/(pi*1i) 2/(3*pi*1i) 2/(5*
   pi*1i) 2/(pi*1i*7) 2/(pi*1i*9)];


conv(conv(harmonics,harmonics),harmonics);
```

k	Magnitudes before tripling	Magnitudes after tripling
-27	-	0.0004
-25	-	0.0014
-23	-	0.0037
-21	-	0.0089
-19	-	0.0243
-17	-	0.0362
-15	-	0.0488
-13	-	0.0639
-11	-	0.0833
-9	0.0707	0.1018
-7	0.0909	0.1200
-5	0.1273	0.1532
-3	0.2122	0.2331
-1	0.6366	0.6485
1	0.6366	0.6485
3	0.2122	0.2331
5	0.1273	0.1532
7	0.0909	0.1200
9	0.0707	0.1018
11	-	0.0833
13	-	0.0639
15	-	0.0488
17	-	0.0362
19	-	0.0243
21	-	0.0089
23	-	0.0037
25	-	0.0014
27	-	0.0004

Figure 18: The change of amplitudes after tripling when the number of harmonics is 9

However, when the signal has a finite bandwidth, bandwidth expansion occurs because of the width property of convolution (Lathi & Ding, 2009). This property states that the bandwidth of the product of two signals, i.e., $g_1(t)$ with bandwidth B_1 and $g_2(t)$ with bandwidth B_1, is B_1+B_2 Thus, if m(t) has a finite bandwidth B_m, a frequency multiplier produces an N-fold expansion, $N \times B_m$. Figure 15 illustrates the expansion of a rectangular pulse in the frequency domain. Consequently, its time-domain representation becomes a sync pulse. The absolute and null-to-null bandwidths of a rectangular pulse increase linearly with the nonlinearity order of the multiplier.

4.2. Constellation Distortion

As shown in Chapter 2, the constellation of an IQ-modulated signal depends only on the amplitude and phase of the modulated waveform, not on its bandwidth. The complex passband representation of IQ modulated signals, given in (2.4), can be modified by incorporating the pulse-shaping function illustrated in Figure 13 to yield the input to the frequency multiplier, V(t). The input to the multiplier is:

$$V(t) = Re\{(V_I + jV_Q)g(t)e^{jw_c t}\} = g(t)(V_I cos(w_c t) - V_Q sin(w_c t)) \tag{4.3}$$

where g(t) is a pulse-shaping function. Using the phasor-addition rule, V(t) can be expressed as a function of a single sinusoid, similar to the approach used in the outphasing technique.

$$V(t) = A_v g(t) cos(w_c t + \Theta_V)$$

$$A_v = \sqrt{{V_I}^2 + {V_Q}^2}$$

$$\Theta_v = arctan\left(\frac{V_Q}{V_I}\right) \tag{4.4}$$

The frequency multiplier model is assumed as in (2.5). The multiplier output then can be written as the power of cosines in the equation.

$$z(t) = \sum_{n=1}^{N} c_n {A_v}^n g^n(t) cos^n(w_c t + \Theta_V) \tag{4.5}$$

(4.5) can be expanded using Chebyshev polynomials (Mathar, 2006).

$$cos^N(w_c t) = \frac{1}{2^{N-1}} \sum_{k=0}^{\lfloor N/2 \rfloor} \binom{N}{k} cos(w_c(N-2k)t) \tag{4.6}$$

Then, the output of frequency multiplier becomes

$$z(t) = \sum_{n=1}^{N} c_n {A_v}^n g^n(t) \frac{1}{2^{N-1}} \sum_{k=0}^{\lfloor N/2 \rfloor} \binom{N}{k} cos(w_c(N-2k)t) \tag{4.7}$$

The second BPF, applied after the frequency multiplier, is centered at Nf_c and has a bandwidth at least as wide as that of $g^N(t)$. It suppresses all harmonics from the first through the (N−1)th, isolating the Nth harmonic. Consequently, the output of the BPF in Figure 13 corresponds to the case of (4.7) with k=0 and n=N.

$$y(t) = \frac{c_N {A_V}^N}{2^{N-1}} g^N(t) cos(N w_c t + N\theta_V) \tag{4.8}$$

The complex passband representation of y(t) is

$$y(t) = \frac{c_N {A_V}^N}{2^{N-1}} g^N(t) Re\{(cos(N\theta_V) + jsin(N\theta_V) e^{jNw_c t}\} \tag{4.9}$$

Applying I/Q demodulation followed by an appropriate matched filter produces the baseband I and Q components at the receiver, as shown in (4.10) and (4.11). A digital demodulation block, such as a vector signal analyzer (VSA), can perform these tasks.

$$V_{I,N} = \frac{{A_V}^N}{2^{N-1}} cos(N\theta_V) \tag{4.10}$$

$$V_{Q,N} = \frac{{A_V}^N}{2^{N-1}} sin(N\theta_V) \tag{4.11}$$

Here, the coefficient c_N is omitted for clarity, as it affects only the amplitude and does not change the phase of signal in the constellation. The I and Q components of the input signal V(t) are given by:

$$V_I = A_V cos(\theta_V) \tag{4.12}$$

$$V_Q = A_V sin(\theta_V) \tag{4.13}$$

Thus, the effect of a frequency multiplier on the constellation of an IQ-modulated signal can be identified by comparing (4.10)–(4.11) with (4.12)–(4.13). In this comparison, each component transforms amplitude and phase, which rotates the constellation symbols because of the multiplier's non-linearity. Figure 19 illustrates this symbol rotation.

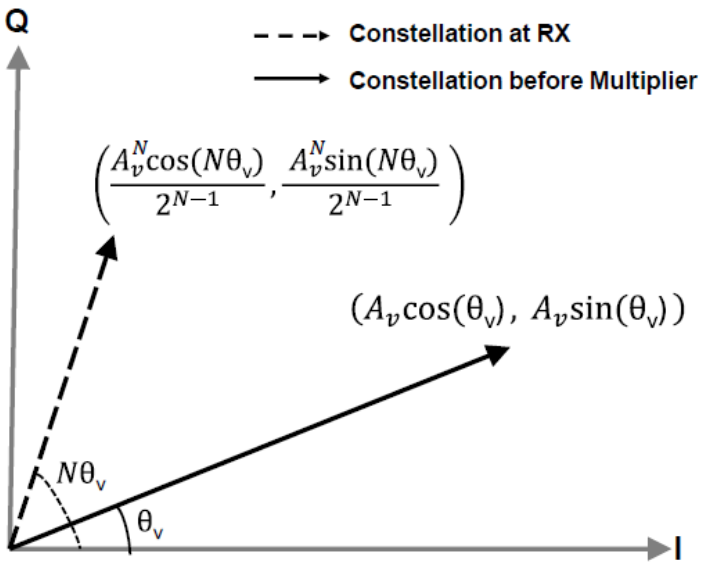

Figure 19: Constellation Distortion due to Frequency Multiplier

QPSK- and 16-QAM-modulated signals were processed with frequency multipliers in the Keysight SystemVue environment to validate the analysis. Figures 20 and 21 illustrate the rotation of the QPSK constellation points when the signal passes through frequency doublers, triplers, and quadruplers.

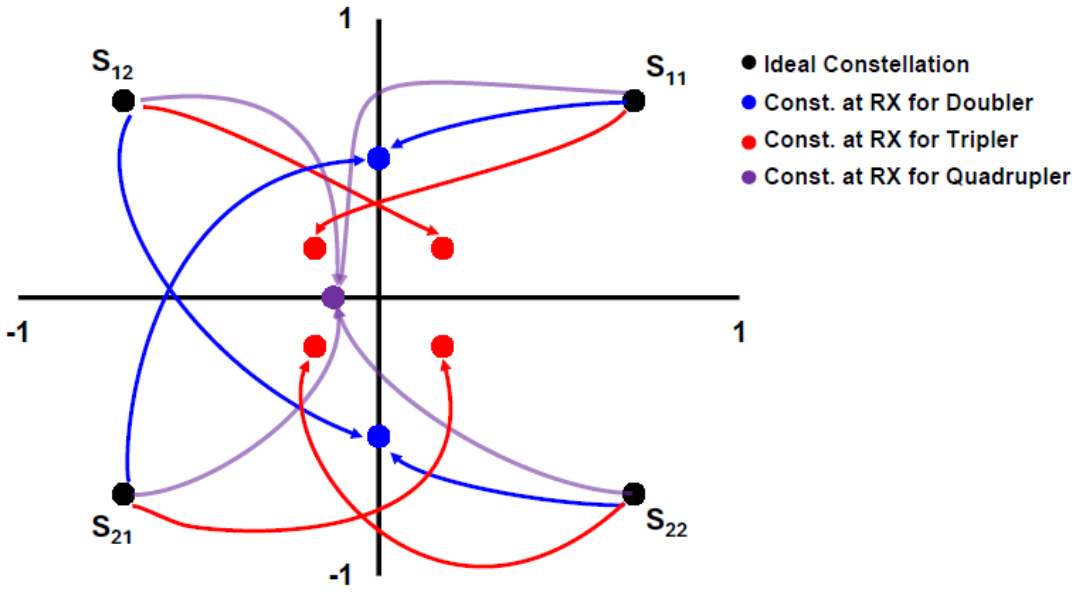

Figure 20: Constellation Distortion due to doubler (N=2), tripler (N=3) and quadrupler (N=4)

Symbol	V_I	V_Q	$V_{I,2}$	$V_{Q,2}$	$V_{I,3}$	$V_{Q,3}$	$V_{I,4}$	$V_{Q,4}$
S_{11}	$\frac{1}{\sqrt{2}}$	$\frac{1}{\sqrt{2}}$	0	$\frac{1}{2}$	$\frac{-1}{4\sqrt{2}}$	$\frac{1}{4\sqrt{2}}$	$\frac{-1}{8}$	0
S_{12}	$-\frac{1}{\sqrt{2}}$	$\frac{1}{\sqrt{2}}$	0	$-\frac{1}{2}$	$\frac{1}{4\sqrt{2}}$	$\frac{1}{4\sqrt{2}}$	$\frac{-1}{8}$	0
S_{21}	$-\frac{1}{\sqrt{2}}$	$-\frac{1}{\sqrt{2}}$	0	$\frac{1}{2}$	$\frac{1}{4\sqrt{2}}$	$\frac{-1}{4\sqrt{2}}$	$\frac{-1}{8}$	0
S_{22}	$\frac{1}{\sqrt{2}}$	$-\frac{1}{\sqrt{2}}$	0	$-\frac{1}{2}$	$\frac{-1}{4\sqrt{2}}$	$\frac{-1}{4\sqrt{2}}$	$\frac{-1}{8}$	0

Figure 21: I and Q coordinates of QPSK symbols for N=2, N=3 and N=4

Figures 20 and 21 confirm the constellation-distortion analysis. The diagram in Figure 20 reveals an interesting case: the symbols overlap after even-order multipliers (e.g., N=2 and N=4). Because of this overlap, unique symbol detection becomes impossible. For equiprobable signals**,** this implies a symbol-error probability of 50 % for the doubler and 75 % for the quadrupler, even in the absence of noise.

Only the tripler preserves unique constellation points, as also demonstrated in Kang et al. (2015). Although the symbols are significantly spread and permuted, this preservation still allows unique detection of each symbol.

The overlap observed with even-order multipliers arises from the four-fold symmetry of the QPSK constellation. Accordingly, the number of unique points remaining after any frequency multiplier can be determined, as in (4.14).

$$M' = \frac{M}{gcd(N, 4)} \tag{4.14}$$

where M is the number of symbols in the input constellation. To verify the discussion above, 16-QAM modulated signals were passed through a doubler, a tripler, and a quadrupler, as shown in Figure 22. The resulting counts of unique constellation points are 8 after the doubler, 16 after the tripler, and 4 after the quadrupler, confirming (4.14).

Consequently, an odd-order multiplier should be used instead of an even-order multiplier to enable unique detection of IQ modulated signals. Note, however, that odd-order multipliers still shrink and permute the decision region for each symbol, which can increase detection sensitivity to noise and impairments.

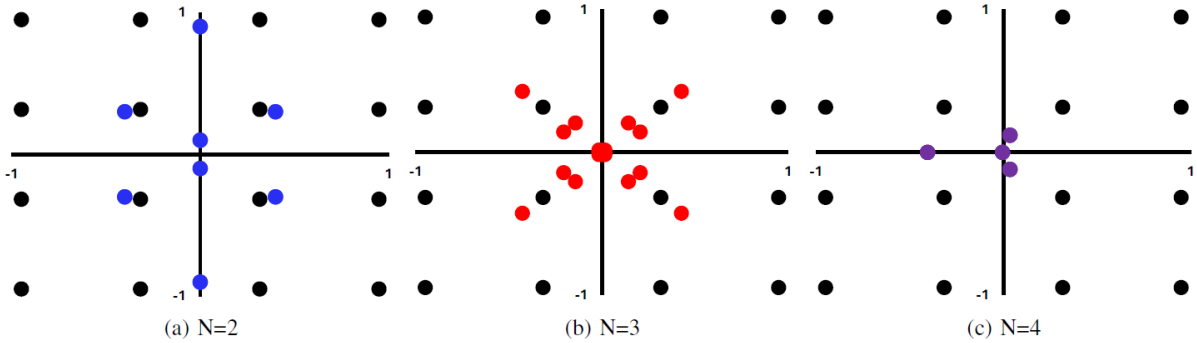

Figure 22: 16-QAM constellation distortion for doubler (a), tripler (b) and quadrupler (c)

4.3. SNR Degradation

As presented in Liu et al. (2015) and Chung et al. (2019), background noise degrades the SNR of the input signal after passing through a frequency multiplier. This observation motivated a system-level analysis of the SNR degradation in IQ-modulated signals following the multiplier. In this analysis, the noisy input to the multiplier is assumed to be:

$$V_\epsilon(t) = V(t) + \epsilon(t) \;=\; A_V g(t) cos(w_c t + \theta_V) \;+\; \epsilon(t) \tag{4.15}$$

Here, ϵ(t) represents the passband AWGN with a flat spectral density of $\frac{N_0}{2}$. The system bandwidth is critical in determining the noise power, which is calculated by integrating the spectral density over the system bandwidth. For instance, if the system has a bandwidth of 2β, the resulting noise power is βN_0.

The noisy output of the frequency multiplier can be given as in (4.15).

$$z_\epsilon(t) = \sum_{n=1}^{N} c_n \big(V(t) + \epsilon(t)\big)^n = z(t) + \sum_{n=1}^{N} c_n \sum_{k=1}^{n} \binom{n}{k} V^{n-k}(t)\epsilon^k(t) \tag{4.16}$$

The result in (4.16) is the sum of the signal and noise terms. By assuming $V(t) >> \epsilon(t)$ (which implies $V^{N-1}(t)\epsilon(t) >> V^{N-2}(t)\epsilon^2(t)$), the noisy output in (4.16) simplifies to the one in (4.17).

$$z_\epsilon(t) \approx z(t) + c_N N V^{N-1}(t)\epsilon(t) \tag{4.17}$$

The Chebyshev expansion can be applied to the noise term in (4.17).

$$c_N N V^{N-1}(t)\epsilon(t) = c_N N \frac{g^{N-1}(t)A_V{}^{N-1}}{2^{N-1}} \sum_{k=0}^{\left\lfloor \frac{N-1}{2} \right\rfloor} \binom{N-1}{k} [\epsilon_I(t)(cos(w_c t(N-2k) + (N-1-2k)\theta_v) + cos(w_c t(N-2-2k) + (N-1-2k)\theta_v)) - \epsilon_Q(t)(sin(w_c t(N-2k) + (N-1-2k)\theta_v) + sin(w_c t(N-2-2k) + (N-1-2k)\theta_v))] \tag{4.18}$$

where the passband representation of the AWGN noise of $\epsilon(t)$ can be shown as

$$\epsilon(t) = \epsilon_I(t)cos(w_c t) - \epsilon_Q(t)sin(w_c t) \tag{4.19}$$

where $\epsilon_I(t)$ and $\epsilon_Q(t)$ denote the I and Q components of the passband noise $\epsilon(t)$. ϵ_I and ϵ_Q are AWGN components, each with spectral density $\beta N_0/2$. The BPF applied after the frequency multiplier isolates the Nth harmonic; as a result, the noisy output of the BPF following the multiplier corresponds to the version of (4.18) for k=0,

$$y_\epsilon(t) = y(t) + \frac{c_N N g^{N-1}(t)A_V{}^{N-1}}{2^{N-1}} \begin{bmatrix} \epsilon_I(t)cos(Nw_c t - (N-1)\theta_V) \\ -\epsilon_Q(t)sin(Nw_c t - (N-1)\theta_V) \end{bmatrix} \tag{4.20}$$

The noisy output in (4.20) has a passband representation

$$y_\epsilon(t) = \frac{c_N A_v{}^N}{2^{N-1}} g^N(t) Re\{(\cos(N\theta_v) + jsin(N\theta_v))e^{j2\pi N f_c t}\} + \frac{c_N N A_v{}^{N-1}}{2^{N-1}} g^{N-1}(t) Re\{(\epsilon_I(t) + j\epsilon_Q(t))e^{j2\pi N f_c t + (N-1)\theta_v}\} \tag{4.21}$$

At the receiver, the noisy output is down-converted into baseband. It becomes

$$\bar{y}_\epsilon(t) = \bar{y}(t) + \bar{\epsilon}(t) = \frac{c_N A_v{}^N}{2^{N-1}} g^N(t)\big(\cos(N\theta_v) + jsin(N\theta_v)\big) + \frac{c_N N A_v{}^{N-1}}{2^{N-1}} g^{N-1}(t) Re\left(\epsilon_I(t) + j\epsilon_Q(t)\right) e^{j2\pi N f_c t + (N-1)\theta_v} \tag{4.21}$$

The SNR of the multiplier output can then be calculated as

$$SNR_{out} = \frac{E[|\bar{y}(t)|^2]}{E[|\bar{\epsilon}(t)|^2]} = \frac{A_v{}^2 P_g}{N_0 \beta N^2} \tag{4.22}$$

where P_g is the power of the pulse shaping function g(t). Considering input SNR,

$$SNR_{in} = \frac{E[|y(t)|^2]}{E[|\epsilon(t)|^2]} = \frac{{A_v}^2 P_g}{N_0 \beta} \tag{4.23}$$

the degradation in SNR due to the N-fold multiplier is equal to,

$$\gamma = 10\log\left(\frac{SNR_{out}}{SNR_{in}}\right) = 10\log\left(\frac{1}{N^2}\right)(dB) \tag{4.24}$$

The analysis shows that the SNR degrades with the square of the multiplier due to the mixing of noise with the input modulated signal. To verify the result obtained in (4.24), a 1 MHz single-tone signal at 0dBm was synthesized and combined with AWGN to form a noisy input. This signal was passed through several frequency multipliers, and the input and output spectra were evaluated using a spectrum analyzer. A simulation bandwidth of 3 MHz was selected to account for the noise power. Figure 23 shows the superimposed spectra for each case.

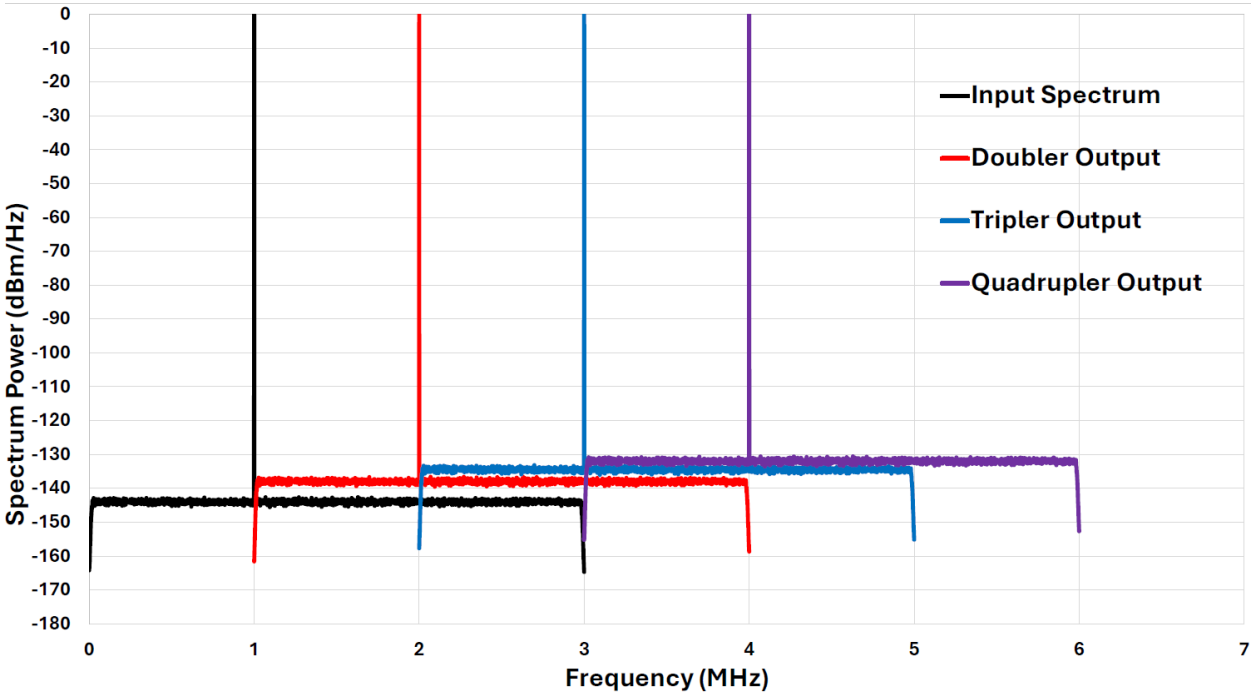

Figure 23: Spectrum of frequency multipliers' input and output signals

The SNR of each spectrum is determined by calculating the signal power and noise power separately and then taking their difference. Figure 24 summarizes the SNR degradation observed in each case.

Multiplier	Input SNR	Output SNR	SNR Degredation
Doubler	79.22	73.22	6
Tripler	79.22	69.68	9.54
Quadrupler	79.22	67.18	12.04

Figure 24: SNR Degradations for Doubler, Tripler, and Quadrupler

These results align perfectly with the analysis, and they confirm previously reported SNR degradation for a frequency quadrupler (Liu et al., (2016)) and generalize the findings to multipliers of any order.

The analysis in subsections 4.2 and 4.3 suggests that a frequency tripler is preferable for digital communications because it preserves the unique detection of symbols while not significantly degrading the SNR. In this configuration, however, a high-frequency mixer is still required to perform frequency upconversion to sub-THz bands.

5. SUMMARY AND DISCUSSION

5.1. Summary of the Thesis

This thesis investigates frequency-multiplier-last transmitters as candidates for sub-THz communication from a digital communications perspective. The Introduction reviews recent advancements in sub-THz transmitter architectures and categorizes them into three types: PA-last, mixer-last, and multiplier-last. The Background section introduces IQ modulation, which is widely used in wireless systems, and presents a modeling approach for frequency multipliers. The Literature Review summarizes recent progress on multiplier-last transmitters and the linearization of frequency multipliers using digital predistortion. Finally, the analysis section presents a comprehensive system-level evaluation of the impairments introduced by frequency multipliers in digital communication chains, specifically addressing bandwidth expansion, constellation distortion, and SNR degradation.

The thesis proposes a novel system-level model for frequency-multiplier-last transmitters to investigate the effect of multipliers to digital communication, aiming to address a gap in the existing literature. The analysis provides insight into the impact of frequency multipliers on digital communication performance, and the derived results are verified through simulation.

5.2. Discussion

As a candidate topology for sub-THz wireless links implemented entirely using CMOS technologies, the frequency-multiplier-last transmitters face significant challenges, primarily due to the low output power resulting from the conversion losses inherent to frequency multipliers where the loss increases proportionally with the order of multiplier. Consequently, such transmitters must rely on multi-antenna configurations or beamforming techniques to enhance communication range.

The analysis, focused on bandwidth expansion, constellation distortion, and SNR degradation, demonstrates that frequency multipliers significantly impair key digital communication metrics. Among multipliers, the tripler provides the best compromise for minimizing degradation of multipliers on digital communication metrics. Nonetheless, frequency-multiplier-last transmitters are generally limited to spectrally inefficient modulation schemes, such as OOK and BPSK, unless mitigation techniques are employed. The outphasing technique offers a potential solution, however it is highly susceptible to IQ mismatches.

Meeting high data-rate requirements specified in the ITU-2030 report necessitates advanced linearization techniques, particularly digital predistortion. However, a fully functional RF frequency-multiplier-last transmitter integrated with wideband DPD has not yet been reported. Additionally, the simultaneous implementation of DPD and antenna solutions in multipliers-last architectures would introduce a significant power penalty which highlights the need for power efficient system-level solutions for practical deployment.

BIBLIOGRAPHY

Abdo, I., Fujimura, T., Miura, T., Tokgöz, K. K., Hamada, H., Nosaka, H., Shirane, A., & Okada, K. (2020). A 300GHz wireless transceiver in 65nm CMOS for IEEE802.15.3d using push-push subharmonic mixer. In *Proc. IEEE MTTS International Microwave Symp*osium, (pp. 623–626).

Abdo, I., Gomez, C. d., Li, Q., Liu, C., Yanagisawa, K., Fadila, A. A., Fujimura, T., Tokgöz, K. K., Pang, J., Hamada, H., Nosaka, H., Shirane, A., & Okada, K. (2022). A bi-directional 300-GHz-band phased-array transceiver in 65-nm CMOS with outphasing transmitting mode and LO emission cancellation. In *IEEE J. Solid-State Circuits 57*(8), 2292–2308.

Badal, M. T. I., Reaz, M. B. I., Bhuiyan, M., & Kamal, N. (2019). CMOS transmitters for 2.4-GHz RF devices: Design architectures of the 2.4-GHz CMOS transmitter for RF devices. In *IEEE Microwave Magazine, 20(3)*, 38-61.

Banerjee, A. (2024). Sub-THz integrated circuits: Challenges and opportunities. In *2024 IEEE 67th International Midwest Symposium on Circuits and Systems (MWSCAS),* (pp. 764-768).

Camargo, E. (1998). *Design of FET frequency multipliers and harmonic oscillators* (1st edition). Artech House.

Chung, A., Darwish, A. M., Viveiros, E., Hung, H. A., Mitran, P., & Boumaiza, S. (2019). Analysis and compensation of nonidealities in frequency-multiplier-based millimeter wave sources. In *IEEE Transactions on Microwave Theory and Techniques 67*(6), 2270-2283.

Darwish, A., Qiu, J., Viveiros, E., Hung, H. A., & Hesler, J. (2016). Efficient linear transmission of complex waveforms at 216 GHz using nonlinear multiplier chains. In *Proc. IEEE MTT-S International Microwave Symposium*, (pp. 1-3).

D'heer, C., & Reynaert, P. (2024). A fully integrated 135-GHz direct-digital 16-QAM wireless and dielectric waveguide link in 28-nm CMOS. In *IEEE Journal of Solid-State Circuits 59*(3), 889-907.

Eissa, M. H., Malignaggi, A., Wang, R., Elkhouly, M., Schmalz, K., Ulusoy, A. C., & Kissinger, D. (2018). Wideband 240-GHz transmitter and receiver in BiCMOS technology with 25-Gbit/s data rate. In *IEEE Journal of Solid-State Circuits 53*(9), 2532-2542.

Fujishima, M. (2013). Power-efficient ultrahigh-speed CMOS wireless communications in terahertz era. In *2013 IEEE International Electron Devices Meeting, 17*(6), 1-4.

Gharaibeh, K. M., Gard, K. G., & Steer, M. B. (2004). Accurate estimation of digital communication system metrics - SNR, EVM and ρ in a nonlinear amplifier environment. In *64th ARFTG Microwave Measurements Conference*, (pp. 41-44)

Gungor, B., & Reynaert, P. (2024). Non-coherent TX-RX chipsets for J-band communication in 16-nm FinFET CMOS. In *IEEE Radio Frequency Integrated Circuits Symposium (RFIC)*, (pp. 75-78).

Heydari, P. (2021). Terahertz integrated circuits and systems for high-speed wireless communications: Challenges and design perspectives. *IEEE Open Journal of the Solid -State Circuits Society*, *1*, 18–36.

International Telecommunication Union. (2015). *Recommendation ITU-R M.2083-0: IMT vision —Framework and overall objectives of the future developments of IMT for 2020 and beyond* (Tech. Rep.). ITU.

International Telecommunication Union. (2023). *Recommendation ITU-R M.2160-0: Framework and overall objectives of the future development of IMT for 2030 and beyond* (Tech. Rep.). ITU.

Jaffri, I., Ayed, A. B., Darwish, A. M., & Boumaiza, S. (2020). High-frequency vector-modulated signal generation using frequency-multiplier-based RF beamforming architecture. In *IEEE/MTT-S International Microwave Symposium (IMS)*, (pp. 551-554).

Kang, S., Thyagarajan, S. V., & Niknejad, A. M. (2015). A 240 GHz fully integrated wideband QPSK transmitter in 65 nm CMOS. In *IEEE J. Solid-State Circuits 50*(10), 2256–2267.

Katayama, K., Takano, K., Amakawa, S., Hara, S., Kasamatsu, A., Mizuno, K., Takahashi, K., & Yoshida, T. (2016), A 300 GHz CMOS transmitter with 32-QAM 17.5 Gb/s/ch capability over six channels. In *IEEE Journal of Solid-State Circuits 51*(12), 3037-3048.

Lathi, B. P., & Ding, Z. (2009). *Modern digital and analog communication systems* (4th ed.). Oxford University Press.

Lee, S., Hara, S., Yoshida, T., Amakawa, S., Dong, R., Kasamatsu, A., Sato, J., & Fujishima, M (2019). An 80-Gb/s 300-GHz-band single-chip CMOS transceiver. In *IEEE Journal of Solid-State Circuits 54*(12), 3577-3588.

Lee, S., Kim, J., Lee, K., & Song, H. J. (2024). 248-GHz subharmonic mixer last transmitter with I/Q imbalance and LO feedthrough calibration. In *IEEE Solid-State Circuits Letters 7*, 159-162.

Liu, Y., Liu, G., & Asbeck, P. M. (2016). High-order modulation transmission through frequency quadrupler using digital predistortion. In *IEEE Transactions on Microwave Theory and Techniques 64*(6), 1896-1910.

Mathar, R. J. (2006). Chebyshev series expansion of inverse polynomials. *Journal of Computational and Applied Mathematics 196*(2), 596–607.

Nopchinda, D., He, Z., Granström, G., Gavell, M., & Zirath, H. (2018). 8-PSK upconverting transmitter using E-band frequency sextupler. In *IEEE Microwave and Wireless Components Letters 28*(2), 177-179.

Pozar, D. M. (2011). *Microwave engineering* (4th ed.). Wiley.

Rodríguez-Vázquez, P., Grzyb, J., Sarmah, N., Heinemann, B., & Pfeiffer, U.R. (2018). A 65 Gbps QPSK one meter wireless link operating at a 225–255 GHz tunable carrier in a SiGe HBT technology. In *2018 IEEE Radio and Wireless Symposium (RWS)* (pp. 146-149).

Rodríguez-Vázquez, P., Grzyb, J., Heinemann, B., & Pfeiffer, U.R. (2019). A 16-QAM 100-Gb/s 1-M wireless link with an EVM of 17% at 230 GHz in an SiGe technology. In *IEEE Microwave and Wireless Components Letters 29*(4), 297-299.

Rodriguez-Vazquez, P., Grzyb, J., Heinemann, B., & Pfeiffer, U. R. (2020). A QPSK 110-Gb/s polarization-diversity MIMO wireless link with a 220–255 GHz tunable LO in a SiGe HBT technology. In *IEEE Transactions on Microwave Theory and Techniques 68*(9), 3834-3851.

Sarmah, N., Vazquez, P. R., Grzyb, J., Foerster, W., Heinemann, B., & Pfeiffer, U. R (2016). A wideband fully integrated SiGe chipset for high data rate communication at 240 GHz. In *11th European Microwave Integrated Circuits Conference (EuMIC)* (pp. 181-184).

Standaert, A., & Reynaert, P. (2020). A 390-GHz outphasing transmitter in 28-nm CMOS. In *IEEE Journal of Solid-State Circuits 55*(10), pp. 2703-2713.

Takano, K., Amakawa, S., Katayama, K., Hara, S., Dong, R., Kasamatsu, A., Hosako, I., Mizuno, K., Takahashi, K., Yoshida, T., & Fujishima, M. (2017). A 105 Gb/s 300 GHz CMOS transmitter. In *IEEE International Solid-State Circuits Conference (ISSCC)*, (pp. 308-309).

Thomas, S., Razavian, S., Virdi, J. S., Sun, W., Motlagh, M. F., & Babakhani, A. (2024). A 400-GHz efficient radiator and OOK transceiver for multi-Gb/s wireless communication in silicon. In *IEEE Journal of Solid-State Circuits 59*(5), 1381-1397.

Tokgöz, K. K., Maki, S., Pang, J., Nagashima, N., Abdo, I., Kawai, S., Fujimura, T., Kawano, Y., Suzuki, T., Iwai, T., Okada, K., & Matsuzawa, A. (2018). A 120Gb/s 16QAM CMOS millimeter-wave wireless transceiver. In *2018 IEEE International Solid-State Circuits Conference (ISSCC)* (pp. 168-170).

Tokgöz, K. K., & Okada, K. (2019). Millimeter-wave CMOS transceiver toward 1Tbps wireless communication. In *2019 IEEE International Symposium on Circuits and Systems (ISCAS)*, (pp. 1-4).

Tripathi, G. C., & Rawat, M. (2023). High-frequency signal generator using cascaded frequency multiplier. In *IEEE Access 11*, 74559-74568.

Wang, Z., Chiang, P. Y., Nazari, P., Wang, C. C., Chen, Z., & Heydari, P. (2014). A CMOS 210-GHz fundamental transceiver with OOK modulation. In *IEEE Journal of Solid-State Circuits*, *49(3)*, 564-580.

Weissberger, A. (2022). June 2022 Ericsson Mobility Report: 5G subscriptions increased by 70 million in Q1-2022 to reach 620 million. *IEEE ComSoc Technology Blog.*

Xu, X., Pan, Y., Lwin, P., & Liang, X. (2011). 3D holographic display and its data transmission requirement. In *2011 International Conference on Information Photonics and Optical Communications,* (pp. 1-4).